Cheng *et al*. *Energy Mater*. **2025**, *5*, 500050
DOI: 10.20517/energymater.2024.142

Energy Materials

Article

Open Access

MOF-derived rose-like carbon-coated Ni-Co phosphide with phosphorus vacancies to enhance hydroxide-ion storage in hybrid supercapacitors

Honghong Cheng[1], Zhibiao Cui[2], Weijie Zheng[2], Dong Shu[2,3,*], Cong Liu[4], Yaotao Zeng[1], Jinyi Zheng[1], Jiayin Cui[1], Keyi Chen[1], Tao Meng[2,*]

[1]School of Chemistry and Materials Science, Guangdong University of Education, Guangzhou 510800, Guangdong, China.
[2]School of Chemistry, South China Normal University, Guangzhou 510006, Guangdong, China.
[3]National and Local Joint Engineering Research Center of MPTES in High Energy and Safety LIBs, South China Normal University, Guangzhou 510006, Guangdong, China.
[4]School of Chemistry, Sun Yat-sen University, Guangzhou 510006, Guangdong, China.

[*]**Correspondence to:** Prof. Dong Shu and Dr. Tao Meng, School of Chemistry, South China Normal University, No. 378, Waihuanxi Road, Guangzhou High Education Mage Center, Panyu District, Guangzhou 510006, Guangdong, China. E-mail: dshu@scnu.edu.cn; mengt@scnu.edu.cn

How to cite this article: Cheng, H.; Cui, Z.; Zheng, W.; Shu, D.; Liu, C.; Zeng, Y.; Zheng, J.; Cui, J.; Chen, K.; Meng, T. MOF-derived rose-like carbon-coated Ni-Co phosphide with phosphorus vacancies to enhance hydroxide-ion storage in hybrid supercapacitors. *Energy Mater*. **2025**, *5*, 500050. https://dx.doi.org/10.20517/energymater.2024.142

Received: 29 Aug 2024 **First Decision:** 14 Nov 2024 **Revised:** 4 Dec 2024 **Accepted:** 12 Dec 2024 **Published:** 21 Feb 2025

Academic Editor: Hao Liu **Copy Editor:** Ping Zhang **Production Editor:** Ping Zhang

Abstract

The low structural stability and sluggish charge-transfer kinetics of transition metal phosphides (TMPs) hinder their application in hybrid supercapacitors. The realization of advanced OH^- storage critically depends on the delicate TMP designs, particularly their chemical composition and structure. Herein, a synergistic engineering approach based on metal-organic framework (MOF)-derived C-coated bimetallic phosphides and P vacancies (Pv) was proposed. Using a Ni-Co-based MOF, a one-step high-temperature carbonization and phosphidation method was employed as the precursor to prepare a rose-like $Ni_{1-x}Co_xP$ composite ($Ni_{1-x}Co$ P@NC), comprising a N-doped carbon (NC) coating and Pv. Physical characterization and theoretical calculations indicated that the open structure with porous $Ni_{1-x}Co_xP$@NC nanosheets originating from high-temperature pyrolysis of Ni-Co-based MOF provides abundant redox-active sites, and the NC layer offers excellent mechanical support for persistent electron/OH^- transfer. The bimetallic phosphides, surface Pv, and NC coating synergistically enhance the electrical conductivity of TMPs, reduce the energy barriers for OH^- adsorption, and accelerate charge-transfer kinetics. The prepared $Ni_{1-x}Co_xP$ @NC electrode possessing an open architecture exhibits a high specific capacitance (2,108 F g^{-1} at 1 A g^{-1}) and excellent rate capability (1,710 F g^{-1} at 10 A g^{-1}). Furthermore, the assembled active carbon//$Ni_{1-x}Co_xP$ P@NC hybrid supercapacitor demonstrates an energy density of 37.7 Wh kg^{-1} at a power density of 750 W kg^{-1}. Our study presents a promising strategy for modifying TMP electrodes to realize efficient and stable OH^- storage in hybrid supercapacitors.

Keywords: Ni-Co bimetallic phosphides, P vacancies, rose-like open structures, OH^- storage, hybrid supercapacitors

INTRODUCTION

Supercapacitors are a rapidly advancing class of energy storage and conversion devices owing to their present superior power density and longer life than those of secondary batteries[1]. The current commercial double-layer supercapacitors exhibit energy densities of < 10 Wh kg^{-1}, and the development of high-energy and high-power density electrode materials is crucial for increasing the application value of supercapacitors[2]. Transition metal phosphides (TMPs) have received widespread attention owing to their advantages concerning electrical conductivity and high capacitance[3,4]. Reportedly, Ni- and Co-based phosphides possessing high electrochemical activity are promising materials for fabricating high-performance supercapacitors[5]. Specifically, Ni-based phosphides possess high capacitance, whereas Co-based phosphides exhibit rapid electrochemical reactions and high structural stability[6-8]. The synergistic effects of bimetallic compounds offer mixed-valence states and richer Faradaic oxidation active sites[9]. Therefore, Ni-Co bimetallic TMPs exhibit considerable potential for realizing favorable electrical conductivity and prolonging the service life compared with monometallic phosphides[10,11]. However, the inherent semiconductor properties and crystal-structural instability of TMPs lead to sluggish electrode kinetics and low cycle stability, substantially hindering their practical energy-storage applications.

Among various structural design strategies, defect engineering is an "inherent" approach for effectively modulating the charge distribution to optimize the electrode reaction kinetics[12,13]. For instance, oxygen vacancies (Ov) have been extensively studied in supercapacitors because they can serve as shallow donors to increase the carrier concentration and conductivity of the active materials[14]. Fu *et al.*[15] prepared yolk-shell-structured MnO_2 microspheres comprising Ov, which exhibited a reduced charge-transfer resistance and a superior rate capability. Coincidentally, introduced P vacancies (Pv) can also create active sites to modulate the electronic structure of the TMPs and reduce the OH^- reaction barrier to enable electron mobility and enhance the electrochemical activity[16,17]. Li *et al.*[17] induced Pv in a CoP@FeP_2 heterostructure via a biotemplate-derived method. Pv substantially influences the abundance of lone pair electrons in the crystal structure, building massive superhighways in the CoP@FeP_2 heterostructure for increasing the electron/OH^- transfer rates within the electrode (1,028.8 F g^{-1} at 5 mV s^{-1}). Zhang *et al.*[18] employed Ar plasma etch lattice-like CoP grown on nickel foam (NF) substrates to adjust the concentration of Pv in the CoP/NF composites. Compared with that of pristine CoP, the capacitance of the sample based on Pv increased by 1.7 times, exhibiting a high capacitance retention rate (90% after 5,000 cycles). These studies reveal that the introduced Pv can not only enhance the intrinsic conductivity of the TMP material but also induce additional active sites to improve OH^- storage capability. However, research on the simultaneous efforts of bimetallic Ni-Co and Pv on the electrochemical properties of TMPs remains insufficient. Additionally, the underlying electrode reaction mechanism in supercapacitors requires further investigation.

In addition to introducing "intrinsic" vacancies in materials, an "extrinsic" strategy has been adopted in recent research. By modulating the TMP morphology or introducing functional conductive components, the electrical conductivity and structural stability of TMPs can be considerably enhanced[19]. Carbon (C)-based conductive networks, such as those based on amorphous carbon[20], carbon nanotubes (CNTs), and graphene, can improve the electron migration ability and alleviate the pulverization of TMPs during the working state[21]. Yi *et al.* synthesized a bimetallic Ni-Co phosphide comprising a N, P codoped C layer (NiCoP/NPC) via an ionic liquid-assisted method[22]. Density functional theory (DFT) calculations revealed that NPC accelerates electron transfer and generates additional active sites. Qian *et al.* prepared a NiCo-phosphide/NiCo layered double oxide CNT composite (NCP/LDO-CNT)[23]. The presence of a small amount of CNTs effectively prevented the self-assembly of NCP/LDO nanosheets into nanoflowers and created abundant electron migration paths, resulting in a good rate capability and structural stability of the NCP/LDO-CNT electrode. However, the aforementioned C sources mostly comprise exogenous carbon, leading to complex synthetic pathways, low dispersion, and weak binding forces between C and the metal components.

In the past decade, metal-organic frameworks (MOFs) have been demonstrated as ideal sacrificial templates for preparing functional nanomaterials[24]. Our research group previously designed functional electrode materials through the MOF derivative method, including a polyhedral star configuration NiS/Co_9S_8 heterojunction[25], hollow sphere functional MnO_2[26], hollow MnO_2 cuboid with active Mn^{3+} and Ov[27], *etc.* Compared with the transition metal oxides and sulfides reported above, MOF-derived Ni-Co bimetallic phosphide/carbon composites have outstanding advantages such as higher electronic conductivity, higher specific capacitance, and enhanced rate capability[28]. From the perspective of material design strategies, metal compound/C composites prepared via the MOF-derived method exhibit the following advantages: (1) high preparation efficiencies and mild conditions; (2) large surface areas and tunable pore structures; (3) highly homogeneous metal compound/C composites after pyrolysis by the periodically arranged organic ligands and metal ions[29]. Thus, NiCoP-based composites with functional C coatings derived from MOFs exhibit superior abilities in addressing the abovementioned intrinsic drawbacks to promote the electrochemical reaction kinetics of NiCoP-based electrodes.

Herein, a synergistic engineering approach based on MOF-derived C-coated bimetallic phosphides and Pv engineering is proposed. The Pv-enriched porous N-doped carbon (NC)-coated $Ni_{1-x}Co_xP$ ($Ni_{1-x}Co_xP$@NC) comprising a blooming rose-like structure was prepared via one-step high-temperature carbonization and phosphidation of Ni-Co-based MOF precursors. This method ensures the uniform and tight binding of the C layer and metal sites, resulting in a porous TMP composite comprising a rose-like morphology and the inherited MOF matrix. The open structure provides abundant redox-active sites, whereas the C framework offers a high-speed electron-transport pathway, ensuring high capacitance and rate capability of the $Ni_{1-x}Co_xP$@NC electrode. Considering the composition design, the synergistic interplay of Co and Ni in the bimetallic phosphides alters the electronic distribution of the metal sites, enhancing the OH^- adsorption ability of the material. Additionally, the introduced Pv synergistically regulates the electronic structure, reducing the reaction barrier and accelerating the charge migrate kinetics in $Ni_{1-x}Co_xP$. The fabricated $Ni_{1-x}Co_xP$@NC electrode exhibits an ultrahigh specific capacitance of 2,108 F g^{-1} at 1 A g^{-1}, reaching 1,699 Fg^{-1} even at 10 A g^{-1} indicating its outstanding rate capability. Furthermore, the hybrid supercapacitor (HSC) assembled using the $Ni_{1-x}Co_xP$@NC anode and active carbon (AC) cathode exhibits a high energy density of 37.7 Wh Kg^{-1} at 750 W Kg^{-1}.

EXPERIMENTAL

Materials

All chemicals were analytically graded and used as received without further purification. Ethanol (AR), ethylene glycol (AR), nickel nitrate tetrahydrate [$Ni(NO_3)_2\cdot 4H_2O$] (AR) and cobalt nitrate hexahydrate [$Co(NO_3)_2\cdot 6H_2O$] (AR) were purchased from Tianjin Damao Chemical Reagent Co., Ltd. Nicotinic acid. (AR) was purchased from Shanghai Macklin Biochemical Co., Ltd. Sodium hypophosphite ($NaH_2PO_2\cdot H_2O$), sodium hydroxide (NaOH) (AR) and N-methyl-pyrrolidone (NMP) were received from Tianjin Zhiyuan Chemical Reagent Co., Ltd.. AC was received from Nanjing Xianfeng Nano Material Technology Co., Ltd.

Synthesis of NiCo-MOF, Ni-MOF and Co-MOF

Typically, 6.4 mmol nicotinic acid, 1 mL deionized water and 0.15 g NaOH were first added in 120 mL mixed solution of ethanol and ethylene glycol (volume ratio = 1:1) under magnetic stirring for 0.5 h. Then 2.66 mmol $Ni(NO_3)_2·4H_2O$ and 1.33 mmol $Co(NO_3)_2·6H_2O$ was added into the above mixture. After vigorous stirring for another 0.5 h, the transparent purple solution was sealed in a 100 mL Teflon-line autoclave and kept at 100 °C for 10 h. The resultant precipitate was collected by centrifugation, washed with ethanol and dried at 60 °C, the product was named as NiCo-MOF. The Ni-MOF, Co-MOF are prepared with the same procedures mentioned above, except the addition amount of metal salt, for the synthesis of Co-MOF and Ni-MOF, the addition amounts of $Co(NO_3)_2·6H_2O$ and $Ni(NO_3)_2·4H_2O$ were adjusted to 4 mmol respectively.

Synthesis of phosphorus vacancies $Ni_{1-x}Co_xP$@NC, Ni_2P@NC and CoP@NC

The N-doped carbon-coated TMP materials with phosphorus vacancies were obtained by one-step high-temperature pyrolysis of MOF precursors. Specifically, 50 mg of the MOF precursor and 150 mg of $NaH_2PO_2·H_2O$ were placed downstream and upstream in a tube. Subsequently, annealed at 500 °C for 2 h under Ar atmosphere with a heating rate of 5 °C min^{-1}. After cooling to room temperature, the final product was successfully prepared. The NiCo-MOF, Co-MOF and Ni-MOF derived materials were named as $Ni_{1-x}Co_xP$@NC, Ni_2P@NC, and CoP@NC, respectively.

RESULTS AND DISCUSSION

The synthesis procedure of the $Ni_{1-x}Co_xP$@NC composite is illustrated in Figure 1A. First, Co^{2+} and Ni^{2+} are subjected to a solvothermal reaction with nicotinic acid in an ethanol/ethylene glycol mixed solution in the presence of trace water and NaOH to obtain NiCo-MOF precursors. Trace water facilitated the dissolution of NaOH in ethanol/ethylene glycol and nicotinic acid deprotonation, thereby promoting crystal nucleation[30]. Scanning electron microscopy (SEM) images [Figure 1B, Supplementary Figure 1A and B] demonstrate that the prepared NiCo-MOF possesses a "blooming rose-like" morphology (diameter≈5 μm), with rose petals comprising 150 nm thick sheets. In contrast, Ni-MOF and Co-MOF prepared using the same method exhibit distinct morphologies [Supplementary Figure 1C-F]. The Ni-MOF presented a uniform "rice-like" morphology (0.3μm × 1.3μm), whereas the Co-MOF demonstrated a "lantern-like" structure (diameter≈10 μm), indicating that the addition of Co^{2+} during Ni-MOF synthesis induces a transition from its original "rice-like" morphology to a lamellar structure similar to the Co-MOF structure. However, different from the closed "lantern-like" Co-MOF structure, the NiCo-MOF nanoflakes subsequently aggregated into "rose-like" open structures. The NiCo-MOF was then employed as sacrificial templates, and $NaH_2PO_2·H_2O$ was utilized as the P source to directly obtain $Ni_{1-x}Co_xP$@NC via a one-step high-temperature pyrolysis[31]. For comparison, the Ni-MOF and Co-MOF precursors were pyrolyzed under the same conditions to obtain Ni_2P@NC and CoP@NC products, respectively. Simultaneously, the PH_3 generated during NaH_2PO_2 decomposition phosphatized the MOF precursor and promoted pore formation in the derivative. SEM images reveal that the $Ni_{1-x}Co_xP$@NC [Figure 1C and Supplementary Figure 2A] and CoP@NC [Supplementary Figure 2B] samples have successfully inherited the morphology of the MOF precursor, indicating the good stability of the structure during the high-temperature treatment. In contrast to the MOF precursor, the "rose petals" of the pyrolyzed $Ni_{1-x}Co_xP$@NC exhibit a uniform porous structure [Figure 1D]. Conversely, Ni_2P@NC [Supplementary Figure 2C] displays an irregular granular morphology. During pyrolysis, the carbonization of nicotinic acid yields an NC conductive network for in situ TMP encapsulations. Transmission electron microscopy (TEM) images [Figure 1E and F, Supplementary Figure 3] reveal that the $Ni_{1-x}Co_xP$ is uniformly coated with an amorphous ~10 nm-thick C layer. As depicted in

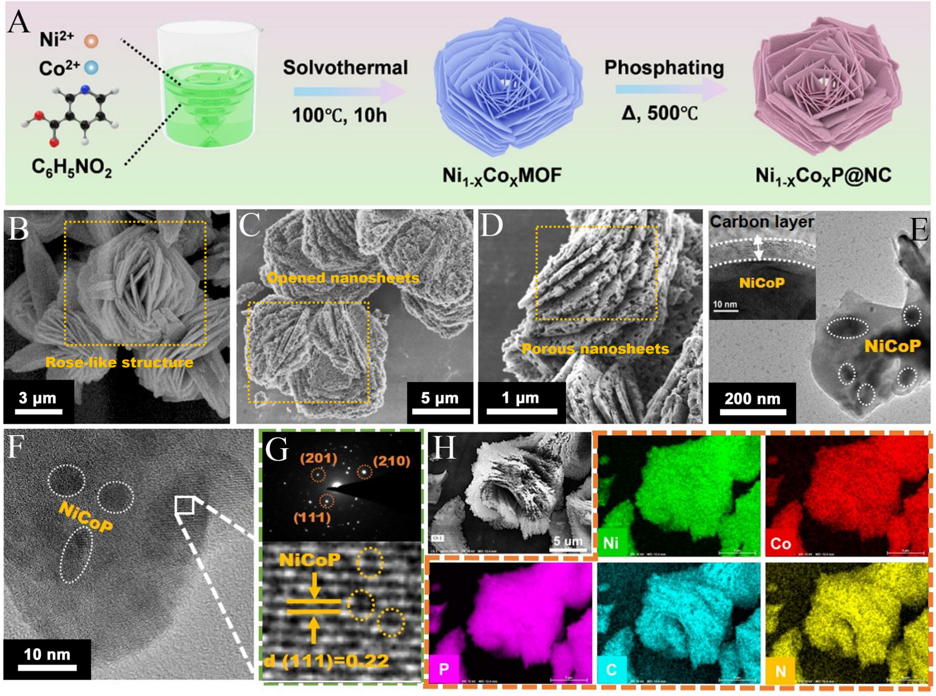

Figure 1. Fabrication and microstructure characterization of $Ni_{1-x}Co_xP$@NC composite. (A) The preparation process of rose-like structure $Ni_{1-x}Co_xP$@NC; SEM images of (C) NiCo-MOF (C and D) $Ni_{1-x}Co_xP$@NC; (E and F) TEM images of $Ni_{1-x}Co_xP$@NC; (G) Selected area electron diffraction patterns (up) and enlarged view of the square in Figure 1F (down); (H) Element mapping images of $Ni_{1-x}Co_xP$@NC. $Ni_{1-x}Co_xP$@NC: N-doped carbon (NC)-coated $Ni_{1-x}Co_xP$; SEM: scanning electron microscopy; MOF: metal-organic frameworks; TEM: transmission electron microscopy.

Figure 1G, the contiguous diffraction rings observed in the selected area electron diffraction (SAED) patterns of the $Ni_{1-x}Co_xP$ sample correspond to the (111), (201), and (210) crystal planes of the NiCoP phase. Additionally, the high-resolution TEM (HR-TEM) images reveal clear lattice fringes with a spacing of 0.22 nm, corresponding to the (111) crystal plane of NiCoP [Figure 1G]. Notably, several lattice vacancies were observed on the NiCoP crystal planes, which can be attributed to the formation of Pv. Elemental mapping results reveal a uniform distribution of Ni, Co, C, P, and N elements in a rose-like opened structure, indicating the molecular-level integration of the C network and $Ni_{1-x}Co_xP$ in the NiCo-MOF derived from lamellar $Ni_{1-x}Co_xP$@NC composite [Figure 1H]. As mentioned earlier, the porous structure of the $Ni_{1-x}Co_xP$@NC material exposes abundant active sites and accelerates the electron/OH^- transfer. Additionally, the uniform NC coating effectively enhances the electron transfer, buffers the volume strain during repeated charge-discharge cycles, and improves the structural stability of the $Ni_{1-x}Co_xP$@NC electrode.

The X-ray diffraction (XRD) patterns [Supplementary Figure 4A] indicate that the phase structure of $Ni_{1-x}Co_xP$@NC is considerably different from that of CoP@NC (PDF#29-0497), but quite similar to that of Ni_2P@NC (PDF#74-1385) [Supplementary Figure 4B]. Specifically, the main diffraction peaks of $Ni_{1-x}Co_xP$@NC observed at 40.7°, 44.5°, 47.3°, and 54.1° are indexed to the (111), (201), (210), and (300) planes of NiCoP, respectively, whereas the broad peak at approximately 25° corresponds to the (002) plane of graphite[32,33], which are consistent with the TEM results. Meanwhile, the peak corresponding to the (002) plane of amorphous graphite appears at the same position in the patterns of the CoP@NC and Ni_2P@NC samples, indicating the successful carbonization of organic ligands in the MOF precursor. According to the inductively coupled plasma (ICP) analysis, the Ni:Co ratio in $Ni_{1-x}Co_xP$@NC is 0.83:0.17; therefore, the chemical composition of $Ni_{1-x}Co_xP$@NC is $Ni_{0.83}Co_{0.17}P$@NC [Supplementary Figure 5]. Supplementary Figure 6 depicts the Raman spectra of $Ni_{1-x}Co_xP$@NC, CoP@NC, and Ni_2P@NC composites, revealing that all the sample spectra comprise two distinct peaks at 1,370 cm^{-1} and 1,580 cm^{-1}, which correspond to the defect (D) and graphitic (G) bands of C, respectively. Notably, the G-to-D band intensity ratio (I_G/I_D ratio) of the samples gradually increases with Co content, suggesting that Co incorporation augments the graphitization degree of C, which is favorable for enhancing the conductivity of the materials[34].

The presence of vacancies was analyzed through electron paramagnetic resonance (EPR) spectroscopy. The broad peak signal ($g \approx 2.0$) depicted in Figure 2A indicates the presence of unpaired electrons, corresponding to Pv in the $Ni_{1-x}Co_xP$@NC, CoP@NC, and Ni_2P@NC samples[35]. The formation mechanism of Pv is speculated as follows: in the preparation of MOFs, the introduction of Co^{2+} causes partial damaged original Ni-MOF crystal structure and introduces a large number of defects[36]. Subsequently, during one-step pyrolysis at 500 °C, the redox reactions led to the partly phosphorus loss of the $Ni_{1-x}Co_xP$@NC material and the phosphorus vacancies were induced[33]. The signal intensity of $Ni_{1-x}Co_xP$@NC was higher than that of CoP@NC and Ni_2P@NC, indicating a larger number of Pv in $Ni_{1-x}Co_xP$@NC; this is mainly because of the increase in the lattice disorder due to the induction of Co atoms in $Ni_{1-x}Co_xP$@NC. The presence of Pv increases the number of lone electron pairs in $Ni_{1-x}Co_xP$@NC, which would form an electronic transmission channel to boost the electrochemical performance. The nitrogen adsorption-desorption isotherms of as-prepared samples are shown in Supplementary Figure 7, the Brunauer-Emmett-Teller (BET) specific surface area (SSA) for $Ni_{1-x}Co_xP$@NC, CoP@NC, and Ni_2P@NC are 4.2, 12.7, 3.0 $m^2\ g^{-1}$, respectively. The SSA of $Ni_{1-x}Co_xP$@NC composites shows improvement over Ni_2P@NC, suggesting that Co incorporation into Ni_2P can partially inhibit Ni_2P from self-aggregation. The N_2 adsorption/desorption isotherms of $Ni_{1-x}Co_xP$@NC reveal a rapid increase in N_2 adsorption volume at high relative pressure ($P/P_0 > 0.9$), suggesting the existence of macropores. Additionally, the pore size distribution indicates that the pores in the $Ni_{1-x}Co_xP$@NC are mainly micropores with a diameter of 1.5 nm. The presence of numerous macropores and mesopores within the structure considerably enhances the mass-transfer capability, whereas the abundant micropores offer extensive space and numerous active sites that are conducive to OH^- adsorption and electrochemical reactions.

X-ray photoelectron spectroscopy (XPS) analysis was used to investigate the surface chemical state of the samples, and the comprehensive spectrum survey confirmed the coexistence of Ni, Co, P, C, and N in the $Ni_{1-x}Co_xP$@NC, which was consistent with the elemental mapping results [Supplementary Figure 8]. Considering the Ni 2p XPS spectra of the $Ni_{1-x}Co_xP$@NC sample, the peaks at 874.9 and 878.2 eV correspond to $2p_{1/2}$, whereas the peak signals at 857.2 and 853.2 eV are attributed to the $2p_{3/2}$ of Ni^{2+} [Figure 2B][37,38]. Similarly, in the Co 2p XPS spectra, two main peaks (798.0 and 782.2 eV) are assigned to $2p_{1/2}$ and $2p_{3/2}$ of the Co^{2+} species. Moreover, two satellite peaks can be detected at 803.4 eV (Co $2p_{1/2}$ Sat.) and 787.5 eV (Co $2p_{3/2}$ Sat.) can also be detected [Figure 2C][39,40]. In the P 2p region, the peaks at approximately 129.6 and 134.1 eV correspond to the P-M ($M=Ni^{2+}$, Co^{2+}) bond and P-O species originating from the oxidation of the sample during preparation [Figure 2D]. The P-O species can effectively alleviate the structural damage during the electrochemical reaction, enhancing the stability of the $Ni_{1-x}Co_xP$. The binding energies in the Ni 2p spectra of $Ni_{1-x}Co_xP$@NC shift to the negative regions (-0.84 and -0.56 eV) compared with those in the Ni_2P@NCs spectra, indicating that more electrons are obtained by the Ni element in the $Ni_{1-x}Co_xP$@NC composite. Combining these findings with the EPR results, the possible reason can be attributed to the presence of a larger number of Pv in the $Ni_{1-x}Co_xP$@NC composite[41]. In addition, the Co 2p spectra of $Ni_{1-x}Co_xP$@NC exhibit a slight positive shift (0.25 eV) compared with that of CoP@NCs. In bimetallic phosphides, the electron affinity of Ni is stronger than that of Co, causing the transfer of electrons from Co to Ni. This electron transfer modifies the electronic structures of the metal

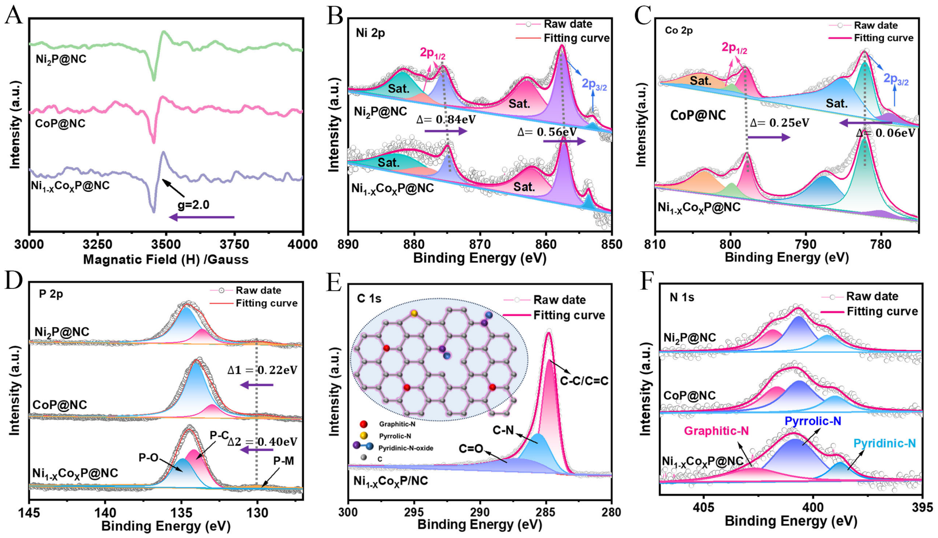

Figure 2. Physical characterization of prepared samples. (A) EPR image of $Ni_{1-x}Co_xP$@NC, Ni_2P@NC and CoP@NC composites. High-resolution XPS spectra of (B) Ni 2p; (C) Co 2p; (D) P 2p; (E) C 1s and (F) N 1s of $Ni_{1-x}Co_xP$@NC, Ni_2P@NC and CoP@NC samples. $Ni_{1-x}Co_xP$@NC: N-doped carbon (NC)-coated $Ni_{1-x}Co_xP$; EPR: electron paramagnetic resonance; XPS: X-ray photoelectron spectroscopy.

atoms, enhancing the electrochemical properties of the $Ni_{1-x}Co_xP$@NC composite[42]. Accordingly, in the $Ni_{1-x}Co_xP$@NC composite, the higher content of Pv brings more free electrons that shift toward the metal ions, leading to a positive shift of the P2p spectra. The charge interaction and redistribution in the $Ni_{1-x}Co_xP$@NC composite are beneficial for inducing a built-in electric field (BIEF) to facilitate electron migration. The C 1s spectra of the $Ni_{1-x}Co_xP$@NC can be divided into the regions of C-C/C=C (284.6 eV), N-C, (285.6 eV), and C=O (287.1 eV) bonds. Further, the inset figure reveals potential N-doping sites within the C lattices[43], confirming the existence of N-C species [Figure 2E]. The peaks at approximately 398.8 eV, 400.8 eV, and 402.7 eV in high-resolution N 1s spectrum are attributed to pyridinic-N, pyrrolic-N, and graphitic-N, respectively [Figure 2F]. Doped-N in the C lattice promotes the interaction between the OH^- solution and the $Ni_{1-x}Co_xP$@NC electrode interface, improving the OH^- storage capability[22,28].

The electrochemical properties of the $Ni_{1-x}Co_xP$@NC composite were evaluated by a three-electrode system in a 6 M KOH solution. The cyclic voltammetry (CV) curve of the $Ni_{1-x}Co_xP$@NC electrode reveals a prominent pair of redox peaks at 0.29 and 0.41 V [Figure 3A] which are derived from its battery-type behavior. The Faradaic redox reactions in the OH^- electrolyte can be given as follows[44,45]:

$$NiCoP + OH^- \leftrightarrow NiCoPOH + e^- \tag{1}$$

$$NiCoPOH + OH^- \leftrightarrow NiCoPO + H_2O + e^- \tag{2}$$

The first step is the oxidation process of NiCoP, and the second stage is the further reaction of NiCoP with OH^- ions to form NiCoPO. During the redox reaction, several different PO phases would be generated and contribute to extra capacitance. The redox peak potentials of the $Ni_{1-x}Co_xP$@NC electrode are between those of the Ni_2P@NC and CoP@NC electrodes, indicating the synergistic effects of Ni and Co on the $Ni_{1-x}Co_xP$@NC electrode[46]. When the scan rate increased from 5 to 50 mV s^{-1}, the CV curves did not exhibit evident deformation, indicating fast OH^- reaction kinetics. The $Ni_{1-x}Co_xP$@NC electrode exhibits the largest CV integral area compared with the Ni_2P@NC and CoP@NC electrodes, indicating that $Ni_{1-x}Co_xP$@NC has a higher specific capacitance and OH^- storage capability than the other samples [Supplementary Figure 9]. It

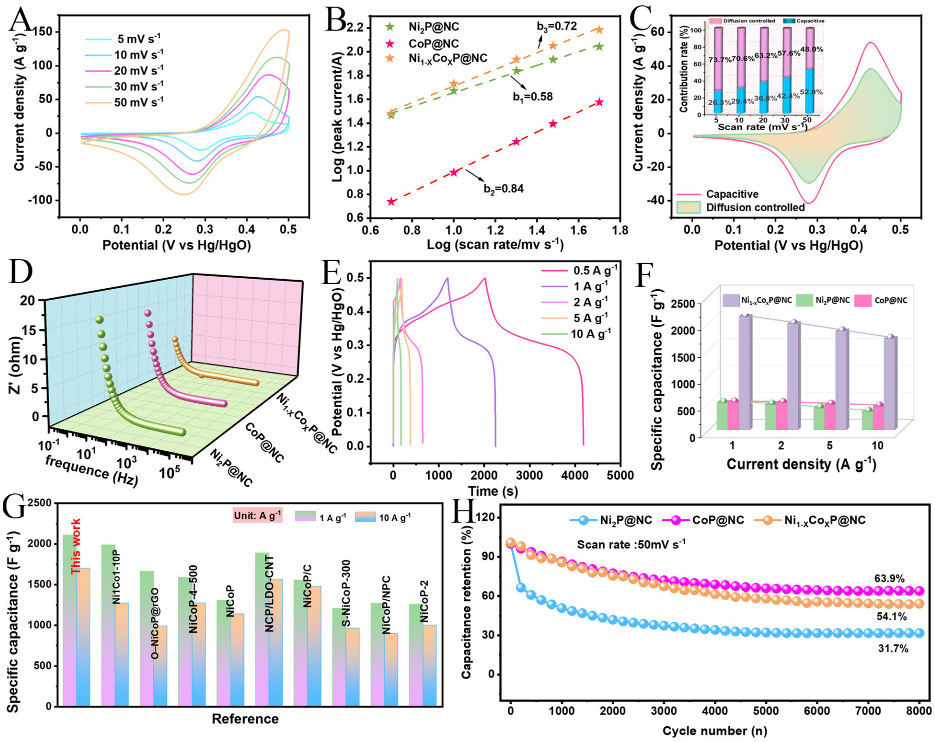

Figure 3. Electrochemical performance of three-electrode system. (A) CV curves of $Ni_{1-x}Co_xP$@NC electrode; (B) Corresponding log (i) vs log (v) plots at specific peaks; (C) Typical diffusion-controlled fraction at 10 mV s^{-1} of the $Ni_{1-x}Co_xP$@NC electrode (inset is the capacitive and diffusion-controlled charge storage at different scan rates); (D) Bode modulus plots; (E) GCD curves of $Ni_{1-x}Co_xP$@NC electrode; (F) Specific capacitance of $Ni_{1-x}Co_xP$@NC, Ni_2P@NC and CoP@NC electrode at different current densities; (G) Comparison of the rate capability with reported NiCo-bimetallic phosphides electrodes; (H) Cycle performance of different electrodes. $Ni_{1-x}Co_xP$@NC: N-doped carbon (NC)-coated $Ni_{1-x}Co_xP$; CV: cyclic voltammetry; GCD: galvanostatic charge/discharge.

can be proved that moderate content of Pv in the electrode would generate an electronic transmission channel, enhance transporting ability of negative charges and further boost pseudocapacitive reaction kinetics. So, the remarkably intensifying energy storage ability of $Ni_{1-x}Co_xP$@NC is attributed to the synergistic effect of nickel-cobalt bimetallic center and Pv. An in-depth analysis of the charge storage mechanism is conducted by calculating the b-value, which represents the relation between log (i) and log (v) obtained from the CV curves. [Figure 3B]. Notably, the b-values of all the electrodes were 0.5-1, indicating that the charge storage process is governed by both capacitive-controlled and diffusion-controlled mechanisms[47]. The b-value of the $Ni_{1-x}Co_xP$@NC electrode (0.72) was between the b-values of the Ni_2P@NC (0.58) and CoP@NC (0.84) electrodes, further confirming the synergistic effects of the Ni-Co bimetallic phosphide. Furthermore, a quantitative analysis was performed at different scan rates. The typical capacitive contribution of $Ni_{1-x}Co_xP$@NC at 10 mV s^{-1} is shown in Figure 3C. The contributions of the capacitive- and diffusion-controlled processes were 29.4% and 70.6%, respectively, indicating that the diffusion-controlled process is dominated at low scan rate. As the scan rate increases, the diffusion-controlled contribution decreases due to ion migration and charge transfer rates failing to keep pace with the change in scan rate. Obviously, as the scan rate increases to 50 mV s^{-1}, the capacitance contribution rises to 52.0%, indicating that the capacitive control becomes dominant at high scan rate. Electrochemical impedance spectroscopy (EIS) analysis demonstrates that all the electrodes exhibit minimal ohmic resistances [Supplementary Figure 10 and Figure 3D]; comparatively, the $Ni_{1-x}Co_xP$@NC electrode has the smallest diffusion internal resistance (R_w: 0.85 Ω) and interfacial charge transfer resistance (R_{ct}: 0.35 Ω) [Supplementary Table 1] and lowest total impedance accumulation at low frequencies

[Figure 3D], indicating that the Pv and NiCo-Bimetallic optimized the internal electronic environment and thereby synergistically enhance the OH^- migration rate of the prepared $Ni_{1-x}Co_xP$@NC materials[48]. When Pv is created in the TMP lattice, the transition metal elements near it are positively charged state, and more electrons can be adsorbed to participate in the redox reaction. After the generation of Pv, the adjacent lattice atoms will form dangling bonds, and these dangling bonds will form an electron transport channel to promote more electrons to participate in the redox reaction, thus further improving the electrochemical performance of $Ni_{1-x}Co_xP$@NC materials.

Galvanostatic charge/discharge (GCD) tests were performed at the rent rates ranging from 1 to 10 A g^{-1} [Figure 3E and Supplementary Figure 11A-C]. When the potential is above 0.4 V, the CV curves of the CoP@NC electrode indicate evident side reactions, and the GCD potential window of the NC electrode is 0.42 V. All the GCD curves exhibit a nonlinear behavior with noticeable potential plateaus, indicating electrochemical battery-type characteristics, which is consistent with the CV results. The IR drop values of the $Ni_{1-x}Co_xP$@NC, Ni_2P@NC and CoP@NC electrodes at 1 A g^{-1} and 10 A g^{-1} were calculated from the GDC results [Supplementary Table 2]. The $Ni_{1-x}Co_xP$@NC electrode shows the smallest IR drop value (0.11 mV) at 10 A g^{-1} (Ni_2P@NC and CoP@NC are 23 and 11 mV, respectively), indicating that $Ni_{1-x}Co_xP$@NC possesses the fastest current response rate. The gravimetric capacitance of the $Ni_{1-x}Co_xP$@NC electrode is 2,108 F g^{-1} at 1 A g^{-1}, whereas the corresponding values of Ni_2P@NC and CoP@NC are 502 and 512 F g^{-1}, respectively [Supplementary Table 2]. Encouragingly, the $Ni_{1-x}Co_xP$@NC electrode demonstrates a relatively excellent capacitance retention of 81.1% at 10 A g^{-1}, compared with the capacitance retention values of Ni_2P@NC and CoP@NC, which are 67.7% and 85.5%, respectively [Figure 3F and Supplementary Figure 12]. The $Ni_{1-x}Co_xP$@NC electrode demonstrates remarkable comprehensive advantages concerning capacitance and rate performance, which is primarily attributed to the synergistic effects of porous rose-liked architecture, NC framework, and BIEF generation in the $Ni_{1-x}Co_xP$@NC[49]. The gravimetric capacitance and rate capability of $Ni_{1-x}Co_xP$@NC are highly competitive with those of the recently reported Ni-Co bimetallic phosphide [Figure 3G and Supplementary Table 3][19,21-23,50-54]. The multiphase interface formed by NC and $Ni_{1-x}Co_xP$ enriched with Pv exhibits strong charge interactions, creating a BIEF that accelerates the charge transport and enhances the electrode reaction kinetics[55]. Additionally, long-term high-rate measurements revealed that the $Ni_{1-x}Co_xP$@NC electrode retained 54.1% of its initial capacitance after 8,000 cycles at 50 mV s^{-1} [Figure 3H], which was substantially higher than that observed for the Ni_2P@NC electrode (31.7%). As shown in Supplementary Figure 13A, the $Ni_{1-x}Co_xP$@NC electrode shows the faint outline of the “rose” after a long-term cycle, but the "rose" petals progressively accumulate owing to the extended electrochemical reaction process. The TEM results [Supplementary Figure 13B and C] reveal that the surface of the $Ni_{1-x}Co_xP$@NC is snugly encapsulated by a carbon layer, whereas the lattice spacing of $Ni_{1-x}Co_xP$@NC has expanded to 0.27 nm, potentially attributable to the repetitive intercalation/deintercalation of electrolyte ions. Furthermore, the SAED pattern [Supplementary Figure 13D] demonstrates that the crystal structure remains well-preserved after extensive cycling, attesting to the chemical stability of $Ni_{1-x}Co_xP$@NC. During cycling, the rose petals supported each other and cushioned the mechanical stress, while the surface NC coating effectively buffered the volumetric strain during long-term cycles, maintaining the structural stability of the $Ni_{1-x}Co_xP$@NC electrode.

To further reveal the intrinsic properties of the as-fabricated samples, the electronic structure and the OH^- reaction kinetics were investigated via DFT calculations. The optimization models for Pv-riched $Ni_{1-x}Co_xP$, $Ni_{1-x}Co_xP$ without Pv, Ni_2P, and CoP are presented in Figure 4A and Supplementary Figure 14. The calculated total density of states (DOS) of Pv-riched $Ni_{1-x}Co_xP$ indicates stronger electron delocalization near the Fermi level than that in $Ni_{1-x}Co_xP$ without P_v, Ni_2P, and CoP, leading to a smaller electronic transition band gap [Figure 4B and Supplementary Figure 15A-C][9,55]. This is primarily attributed to the

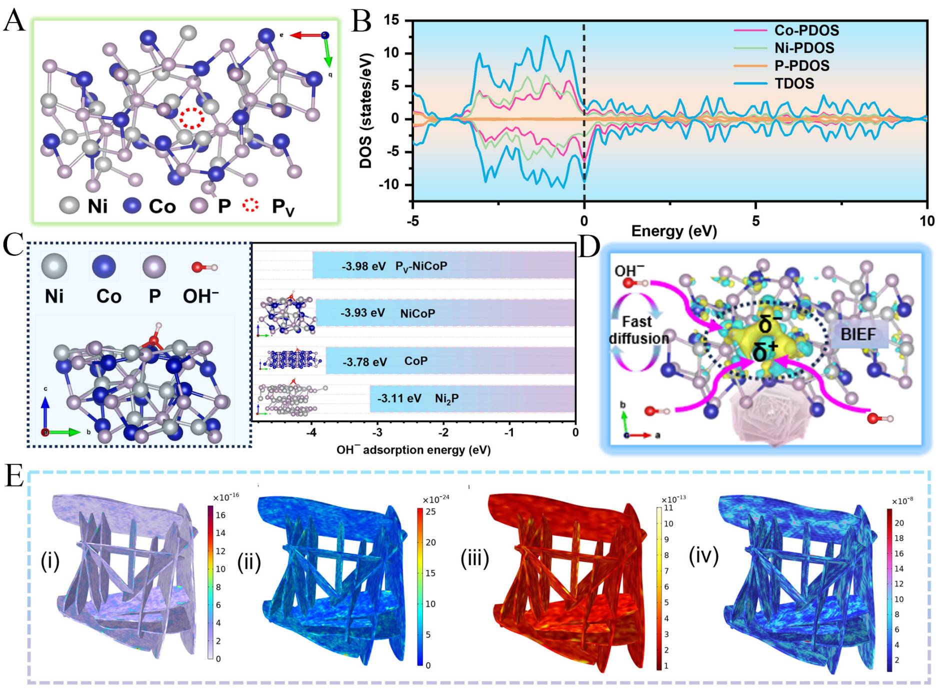

Figure 4. Theoretical calculations and physical simulations. (A) Optimized model of and (B) total DOS stimulation of Pv-riched $Ni_{1-x}Co_xP$; (C) The adsorption model and the comparison of adsorption energies of OH^- among Pv-riched $Ni_{1-x}Co_xP$, $Ni_{1-x}Co_xP$ without Pv, Ni_2P and CoP; (D) Schematic illustration of enhanced reaction kinetics of $Ni_{1-x}Co_xP$@NC electrode in OH^- electrolyte; (E) Simulations of (i) electric field, (ii) charge density distribution, (iii) temperature difference and (iv) structure deformation in $Ni_{1-x}Co_xP$@NC composite (0.5 V). $Ni_{1-x}Co_xP$@NC: N-doped carbon (NC)-coated $Ni_{1-x}Co_xP$; DOS: density of states; Pv: P vacancies.

BIEF induced by the Pv and the synergistic effects of the bimetallic components. The determination of adsorption energy is crucial for understanding the redox reaction kinetics and OH^- transfer efficiency between the active material and the electrolyte. Figure 4C shows the OH^- adsorption energies for the Pv-rich $Ni_{1-x}Co_xP$, $Ni_{1-x}Co_xP$ without Pv, Ni_2P, and CoP surfaces are -3.98, -3.93, -3.11, and -3.78 eV, respectively, demonstrating that the synergistic effects between the Ni-Co bimetallic components and Pv can decrease the energy barriers of OH^- diffusion and improve the rate capability of the $Ni_{1-x}Co_xP$@NC electrode. The charge distribution of $Ni_{1-x}Co_xP$ is shown in Supplementary Figure 16, confirming that the presence of Pv can effectively adjust the charge distribution. The local BIEF is formed around the Pv, which results in an unbalanced charge distribution and generates positively and negatively charged regions, producing the driving force for electron/OH^- migration[56,57]. Therefore, the OH^- reaction kinetic mechanism of the Pv-rich $Ni_{1-x}Co_xP$@NC electrode has been proposed [Figure 4D]. Prior to charging, owing to its potent adsorption capability, the Pv-rich $Ni_{1-x}Co_xP$@NC material captures abundant OH^-, ensuring an ample supply of reacting substances for the electrode reaction. Once charging commences, the BIEF induced by the Pv and the synergistic effects of the NC framework accelerates the electron transfer, boosting the surface reaction of OH^-. Such an advanced mechanism maintains the stable operation of electron/OH^-, considerably accelerating the kinetic process of the $Ni_{1-x}Co_xP$@NC electrode in the OH^--based electrolyte.

COMSOL simulations were performed to further explore the physical properties of the $Ni_{1-x}Co_xP$@NC composite. Figure 4E (i) demonstrates that the electric field distribution in the $Ni_{1-x}Co_xP$@NC material is uniform, and strong localized electric fields are not observed. Figure 4E (ii) reveals that a substantial amount of charge is distributed across the surface of the material sheets during the electrode reaction process, indicating the presence of numerous active sites and demonstrating the superior energy-storage capability.

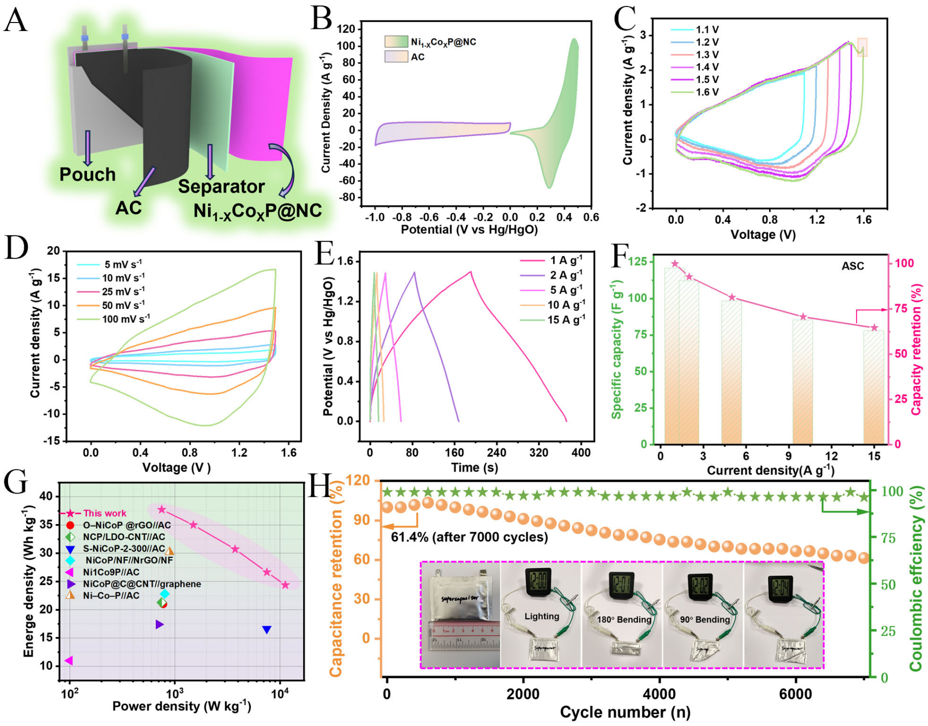

Figure 5. Electrochemical properties of AC//$Ni_{1-x}Co_xP$@NC hybrid supercapacitor. (A) Schematic illustration of AC//$Ni_{1-x}Co_xP$@NC; (B) CV curves of $Ni_{1-x}Co_xP$@NC and AC electrodes in a three-electrode system; (C) CV curves of AC//$Ni_{1-x}Co_xP$@NC in different potential windows at 10 mV s^{-1}; (D) CV curves and (E) GCD curves; (F) Rate capability; (G) Ragone plots of AC//$Ni_{1-x}Co_xP$@NC with reported Ni-Co bimetallic phosphides-based HSC; (H) Cycle performance at 15 A g^{-1} [inset (left to right): is the external dimensions of AC//$Ni_{1-x}Co_xP$@NC HSC pouch; AC//$Ni_{1-x}Co_xP$@NC HSC pouch keep stable power output under 0°-180° bending and cutting states]. AC: Active carbon; $Ni_{1-x}Co_xP$@NC: N-doped carbon (NC)-coated $Ni_{1-x}Co_xP$; CV: cyclic voltammetry; GCD: galvanostatic charge/discharge; HSC: hybrid supercapacitor.

Furthermore, the temperature of the $Ni_{1-x}Co_xP$@NC material remained relatively stable throughout the electrochemical reaction, effectively mitigating the high resistance effects typically associated with localized overheating [Figure 4E (iii)]. Finally, a uniform stress distribution was experienced by the $Ni_{1-x}Co_xP$@NC material sheets, indicating that the deformation induced by volume expansion is restricted [Figure 4E (iv)]. The open nanosheet structure can provide good mechanical properties and support each other to reduce the expansion strain caused by the localized stress concentration. The simulation results indicate that the $Ni_{1-x}Co_xP$@NC material exhibits strong electrochemical activity and structural stability, which is consistent with the aforementioned results of the electrochemical and DFT calculations analyses.

To explore the practical application potential of $Ni_{1-x}Co_xP$@NC, a pouch-type HSC device was fabricated employing $Ni_{1-x}Co_xP$@NC and AC as the positive and negative electrodes, respectively [Figure 5A]. The charge balance between the positive and negative electrodes in the AC is regulated by adjusting the mass ratio of the constituent materials. The corresponding CV curves are displayed in Figure 5B. As shown in Figure 5C, when the voltage window is 0-1.6 V, considerable oxygen evolution is observed in the anode region of the CV curve. Therefore, the operating voltage of 0-1.5 V was used for the electrochemical analysis of the AC//$Ni_{1-x}Co_xP$@NC HSC. The CV profiles of the AC//$Ni_{1-x}Co_xP$@NC HSC exhibited pronounced redox peaks [Figure 5D], indicating the battery-type mechanism of the device. Despite the increase in the scan rate to 100 mV s^{-1}, the shapes persevered without deterioration, suggesting robust OH^-/electron diffusion capabilities inherent to the HSC. The GCD curve of the AC//$Ni_{1-x}Co_xP$@NC HSC shows symmetric shapes, revealing a high Coulombic efficiency [Figure 5E], and the specific capacitances are 121, 112, 98, 85, and 78 F g^{-1} at 1, 2, 5, 10, and 15 A g^{-1}, respectively, suggesting that the AC//$Ni_{1-x}Co_xP$@NC possesses a superior OH^- storage ability [Figure 5F]. The AC//$Ni_{1-x}Co_xP$@NC HSC shows relatively low resistance [Supplementary Figure 17]. The Ragone plot obtained based on the GCD test results reflects the relationship between the power and energy densities of the HSC [Figure 5G]. The assembled AC//$Ni_{1-x}Co_xP$@NC HSC demonstrates a high energy density of 37.7 Wh kg^{-1} at a power density of 750 W kg^{-1}, maintaining 24.3 Wh k g^{-1} even at 11,250 W kg^{-1}, which is better than that of the previously reported Ni-Co bimetallic phosphides-based devices [Figure 5G and Supplementary Table 4][23,50,52,53,58-60]. These results reveal the excellent energy storage performance of the AC//$Ni_{1-x}Co_xP$@NC HSC. Furthermore, the HSC exhibits long-term high-rate cycle stability, maintaining over 64.1% of its capacitance after 7,000 cycles even at a high current density of 15 A g^{-1}. The prepared HSC device can easily power a digital clock in the 0°-180° folded states and maintain a stable power output after folding [Figure 5H], clearly evidencing the application potential of the $Ni_{1-x}Co_xP$@NC composite as a battery-type electrode for HSCs.

CONCLUSIONS

In summary, this study presents a strategy based on the MOF-derived method for constructing $Ni_{1-x}Co_xP$@NC with Pv as a supercapacitor material for advanced OH^- storage. The energy storage mechanism of $Ni_{1-x}Co_xP$@NC was revealed in detail by DFT calculation and physical simulation, and the effect of synergistic interaction between Ni-Co bimetal and Pv on electrochemical properties of TMPs was systematically studied. The exceptional energy storage performance of $Ni_{1-x}Co_xP$@NC is attributed to the open architecture, NC framework, abundant Pv, and the synergistic effects of the bimetallic phosphides. Per experimental, the combination of bimetallic phosphides and Pv induces a BIEF on the $Ni_{1-x}Co_xP$ surface, significantly reducing the adsorption energy barrier for OH^-. Additionally, Pv and NC synergistically modulate the electronic distribution and improve conductivity. Furthermore, the open structure of the $Ni_{1-x}Co_xP$ sheets and the NC coating layer buffer the volumetric expansion during the repeated charge/discharge process. The $Ni_{1-x}Co_xP$@NC electrode delivers a high capacitance of 2,108 F g^{-1} and excellent rate capability (1,710 F g^{-1} at 10 A g^{-1}). The $Ni_{1-x}Co_xP$@NC can serve as a cathode material for high energy and power density HSC. It is expected to further enhance the performance of HSC and meet the needs of a wider range of applications. This study emphasizes the impact of structural design and surface defect engineering on boosting the supercapacitive performance of TMP materials. We believe that this work not only presents a novel methodology for designing TMP structures and compositions, but also serves as a source of guidance and inspiration for future endeavors in the realm of energy storage and conversion.

DECLARATIONS

Authors' contributions

Conceived the idea of this study and designed the experiments: Cheng, H.; Cui, Z.; Meng, T.

Performed the material synthesis: Cheng, H.

Contributed to the XRD, SEM, TEM, ICP-OES, N_2 adsorption/desorption measurements, EPR and XPS characterization: Cheng, H.; Meng, T.; Cui, Z.; Zheng, W.; Liu, C.; Zeng, Y.; Zheng, J.; Cui, J.; Chen, K.

COMSOL simulations: Zheng, W.

Analyzed the data and wrote the paper: Cheng, H.; Cui, Z.; Meng, T.; Shu, D.

Supervision, funding acquisition: Cheng, H.; Meng, T.; Shu, D.

All authors have read and agreed to the published version of the manuscript.

Availability of data and materials

Data will be made available upon reasonable request to the corresponding author.

Financial support and sponsorship

The authors wish to acknowledge the following financial supporters of this work: Youth Innovation Talents Project of Guangdong Universities (natural science) (2023KQNCX052); the National Natural Science Foundation of China (Grant No. 22409065); Guangdong Basic and Applied Basic Research Foundation (2022A1515011906); the Postdoctoral Fellowship Program of CPSF (GZC20230868).

Conflicts of interest

All authors declared that there are no conflicts of interest.

Ethical approval and consent to participate

Not applicable.

Consent for publication

Not applicable.

Copyright

REFERENCES

1. Zhang, Y.; Mei, H.; Cao, Y.; et al. Recent advances and challenges of electrode materials for flexible supercapacitors. *Coord. Chem. Rev.* **2021**, *438*, 213910. DOI
2. Da, S. L. M.; Cesar, R.; Moreira, C. M.; et al. Reviewing the fundamentals of supercapacitors and the difficulties involving the analysis of the electrochemical findings obtained for porous electrode materials. *Energy. Storage. Mater.* **2020**, *27*, 555-90. DOI
3. Acharya, D.; Pathak, I.; Dahal, B.; et al. Immoderate nanoarchitectures of bimetallic MOF derived Ni-Fe-O/NPC on porous carbon nanofibers as freestanding electrode for asymmetric supercapacitors. *Carbon* **2023**, *201*, 12-23. DOI
4. Zhu, Y.; Lu, P.; Li, F.; Ding, Y.; Chen, Y. Metal-rich porous copper cobalt phosphide nanoplates as a high-rate and stable battery-type cathode material for battery-supercapacitor hybrid devices. *ACS. Appl. Energy. Mater.* **2021**, *4*, 3962-74. DOI
5. Zhang, Y.; Jing, X.; Yan, X.; et al. Rational design of NiMn-based electrode materials for high-performance supercapacitors. *Coord. Chem. Rev.* **2024**, *499*, 215494. DOI
6. Patil, S. S.; Patil, P. S. Status review of nickel phosphides for hybrid supercapacitors. *Nanoscale* **2022**, *14*, 16731-48. DOI PubMed
7. Wen, J.; Xu, B.; Zhou, J. Toward flexible and wearable embroidered supercapacitors from cobalt phosphides-decorated conductive fibers. *Nanomicro. Lett.* **2019**, *11*, 89. DOI PubMed PMC
8. Nallapureddy, J.; Pallavolu, M. R.; Srinivasa, B. P. S.; Al-asbahi, B. A.; Joo, S. W. Designed construction of hierarchical cobalt sulfide nanonetwork as a high-capacity and binder-free cathode for hybrid supercapacitors. *Energy. Fuels.* **2023**, *37*, 17535-44. DOI
9. Wu, Y.; Tao, X.; Qing, Y.; et al. Cr-doped FeNi-P nanoparticles encapsulated into N-doped carbon nanotube as a robust bifunctional catalyst for efficient overall water splitting. *Adv. Mater.* **2019**, *31*, e1900178. DOI
10. Zhao, Z.; Miao, Y.; Lu, Q. Electrospun nickel cobalt phosphide/carbon nanofibers as high-performance electrodes for supercapacitors. *J. Power. Sources.* **2024**, *606*, 234587. DOI
11. Hussain, N.; Abbas, Z.; Ansari, S. N.; Kedarnath, G.; Mobin, S. M. Phosphorization engineering on a MOF-derived metal phosphide heterostructure (Cu/Cu_3P@NC) as an electrode for enhanced supercapacitor performance. *Inorg. Chem.* **2023**, *62*, 17083-92. DOI
12. Lu, W.; Yan, L.; Ye, W.; Ning, J.; Zhong, Y.; Hu, Y. Defect engineering of electrode materials towards superior reaction kinetics for high-performance supercapacitors. *J. Mater. Chem. A.* **2022**, *10*, 15267-96. DOI
13. Zhang, Y.; Tao, L.; Xie, C.; et al. Defect engineering on electrode materials for rechargeable batteries. *Adv. Mater.* **2020**, *32*, e1905923. DOI
14. Zhang, A.; Gao, R.; Hu, L.; et al. Rich bulk oxygen vacancies-engineered MnO_2 with enhanced charge transfer kinetics for supercapacitor. *Chem. Eng. J.* **2021**, *417*, 129186. DOI
15. Fu, Y.; Gao, X.; Zha, D.; Zhu, J.; Ouyang, X.; Wang, X. Yolk-shell-structured MnO_2 microspheres with oxygen vacancies for high-performance supercapacitors. *J. Mater. Chem. A.* **2018**, *6*, 1601-11. DOI
16. Hong, Z.; Zhang, S.; Xia, Y.; et al. Nickel-doped cobalt phosphide with phosphorus-vacancy-abundant as an efficient catalyst for non-aqueous and quasi-solid-state Li-O_2 batteries. *Mater. Today. Energy.* **2024**, *43*, 101597. DOI
17. Li, K.; Guo, Z.; Sun, Q.; et al. Phosphorus vacancy regulation and interfacial coupling of biotemplate derived CoP@FeP_2 heterostructure to boost pseudocapacitive reaction kinetics. *Chem. Eng. J.* **2023**, *454*, 140223. DOI
18. Zhang, Q.; Zhang, W.; Ma, X.; et al. Boosting pseudocapacitive energy storage performance via both phosphorus vacancy defect and charge injection technique over the CoP electrode. *J. Alloys. Compd.* **2021**, *864*, 158106. DOI
19. Wang, X.; Li, W.; Xu, Y.; et al. NiCoP/C composite with hollow sphere as electrodes for high performance supercapacitors.

Electrochim. Acta. **2022**, *434*, 141313. DOI

20. Tian, W.; Ren, P.; Hou, X.; et al. MnO_2 porous carbon composite from cellulose enabling high gravimetric/volumetric performance for supercapacitor. *Int. J. Biol. Macromol.* **2024**, *261*, 129977. DOI
21. Zhang, H.; Guo, H.; Zhang, J.; et al. NiCo-MOF directed NiCoP and coconut shell derived porous carbon as high-performance supercapacitor electrodes. *J. Energy. Storage.* **2022**, *54*, 105356. DOI
22. Yi, M.; Lu, B.; Zhang, X.; et al. Ionic liquid-assisted synthesis of nickel cobalt phosphide embedded in N, P codoped-carbon with hollow and folded structures for efficient hydrogen evolution reaction and supercapacitor. *Appl. Catal. B. Environ.* **2021**, *283*, 119635. DOI
23. Qian, J.; Sun, L.; Shi, X.; et al. Dispersive NiCoP/LDO heterostructure nanosheets scattered by CNTs enabling high-performance electrochemical energy storage. *Chem. Eng. J.* **2022**, *429*, 132482. DOI
24. Du, M.; Geng, P.; Feng, W.; Xu, H.; Li, B.; Pang, H. In situ phosphorization for constructing Ni_5P_2-Ni heterostructure derived from bimetallic MOF for Li-S batteries. *Small* **2024**, *20*, e2401587. DOI
25. Cui, Z.; Zheng, W.; Meng, T.; et al. Molecular level heterojunction with sulfur vacancy of stable polyhedral star configuration for boosting hydroxide ion storage. *Energy. Storage. Mater.* **2024**, *71*, 103681. DOI
26. Li, Q.; Gao, A.; Meng, T.; et al. Metal-organic framework derived functional MnO_2 via an in-situ oxidation strategy for advanced quasi-solid-state supercapacitors. *J. Power. Sources.* **2023**, *560*, 232705. DOI
27. Ling, J.; Gao, A.; Huang, Y.; et al. Self-templated and triethanolamine-induced hollow MnO_2 nanoboxes with abundant active Mn^{3+} and oxygen vacancies for high-performance Na-ion pseudocapacitors. *Chem. Eng. J.* **2023**, *452*, 139661. DOI
28. Wang, G.; Yi, F.; Zhong, J.; et al. Towards high-performance supercapacitor electrodes via achieving 3D cross-network and favorable surface chemistry. *ACS. Appl. Mater. Interfaces.* **2022**, *14*, 34637-48. DOI
29. Shen, K.; Chen, X.; Chen, J.; Li, Y. Development of MOF-derived carbon-based nanomaterials for efficient catalysis. *ACS. Catal.* **2016**, *6*, 5887-903. DOI
30. Li, J.; Yan, D.; Hou, S.; Lu, T.; Yao, Y.; Pan, L. Metal-organic frameworks converted flower-like hybrid with Co_3O_4 nanoparticles decorated on nitrogen-doped carbon sheets for boosted lithium storage performance. *Chem. Eng. J.* **2018**, *354*, 172-81. DOI
31. Zhang, N.; Li, Y.; Xu, J.; et al. High-performance flexible solid-state asymmetric supercapacitors based on bimetallic transition metal phosphide nanocrystals. *ACS. Nano.* **2019**, *13*, 10612-21. DOI
32. Lin, Y.; Chen, X.; Tuo, Y.; Pan, Y.; Zhang, J. In-situ doping-induced lattice strain of NiCoP/S nanocrystals for robust wide pH hydrogen evolution electrocatalysis and supercapacitor. *J. Energy. Chem.* **2022**, *70*, 27-35. DOI
33. Wang, X.; Liu, X.; Wu, S.; et al. Phosphorus vacancies enriched cobalt phosphide embedded in nitrogen doped carbon matrix enabling seawater splitting at ampere-level current density. *Nano. Energy.* **2023**, *109*, 108292. DOI
34. Yang, H.; Xiong, T.; Zhu, Z.; et al. Deciphering the lithium storage chemistry in flexible carbon fiber□based self□supportive electrodes. *Carbon. Energy.* **2022**, *4*, 820-32. DOI
35. Lin, J.; Yan, Y.; Xu, T.; et al. Rich P vacancies modulate Ni_2P/Cu_3P interfaced nanosheets for electrocatalytic alkaline water splitting. *J. Colloid. Interface. Sci.* **2020**, *564*, 37-42. DOI
36. Jiang, L.; Jiang, L.; Luo, X.; et al. Iron-induced vacancy and electronic regulation of nickle phosphides for ampere-level alkaline water/seawater splitting. *Chem. Eng. J.* **2024**, *502*, 157952. DOI
37. Ding, H.; Xu, L.; Wen, C.; et al. Surface and interface engineering of MoNi alloy nanograins bound to Mo-doped NiO nanosheets on 3D graphene foam for high-efficiency water splitting catalysis. *Chem. Eng. J.* **2022**, *440*, 135847. DOI
38. Qian, Q.; Zhang, J.; Li, J.; et al. Artificial heterointerfaces achieve delicate reaction kinetics towards hydrogen evolution and hydrazine oxidation catalysis. *Angew. Chem. Int. Ed.* **2021**, *60*, 5984-93. DOI
39. Li, Y.; Liu, J.; Chen, C.; Zhang, X.; Chen, J. Preparation of NiCoP hollow quasi-polyhedra and their electrocatalytic properties for hydrogen evolution in alkaline solution. *ACS. Appl. Mater. Interfaces.* **2017**, *9*, 5982-91. DOI
40. Zhang, X.; Xue, H.; Sun, J.; et al. Synergy of phosphorus vacancies and build-in electric field into NiCo/NiCoP mott-schottky integrated electrode for enhanced water splitting performance. *Chinese. Chem. Lett.* **2024**, *35*, 108519. DOI
41. Sun, R.; Bai, Y.; Bai, Z.; et al. Phosphorus vacancies as effective polysulfide promoter for high□energy□density lithium-sulfur batteries. *Adv. Energy. Mater.* **2022**, *12*, 2102739. DOI
42. Li, C.; Zhang, H.; Liu, M.; Lang, F.; Pang, J.; Bu, X. Recent progress in metal-organic frameworks (MOFs) for electrocatalysis. *Ind. Chem. Mater.* **2023**, *1*, 9-38. DOI
43. Han, Q.; Zhao, X.; Luo, Y.; et al. Synergistic binary Fe-Co nanocluster supported on defective tungsten oxide as efficient oxygen reduction electrocatalyst in zinc-air battery. *Adv. Sci.* **2022**, *9*, e2104237. DOI
44. Wang, X.; Jing, C.; Zhang, W.; et al. One-step phosphorization synthesis of CoP@NiCoP nanowire/nanosheet composites hybrid arrays on Ni foam for high-performance supercapacitors. *Appl. Surf. Sci.* **2020**, *532*, 147437. DOI
45. Li, X.; Elshahawy, A. M.; Guan, C.; Wang, J. Metal phosphides and phosphates-based electrodes for electrochemical supercapacitors. *Small* **2017**, 13. DOI
46. Xu, W.; Wang, T.; Wang, H.; et al. Free-standing amorphous nanoporous nickel cobalt phosphide prepared by electrochemically delloying process as a high performance energy storage electrode material. *Energy. Storage. Mater.* **2019**, *17*, 300-8. DOI
47. Zhang, G.; Hu, J.; Nie, Y.; et al. Integrating flexible ultralight 3D Ni micromesh current collector with NiCo bimetallic hydroxide for smart hybrid supercapacitors. *Adv. Funct. Mater.* **2021**, *31*, 2100290. DOI
48. Ren, X.; Li, M.; Qiu, L.; et al. Cationic vacancies and interface engineering on crystalline-amorphous gamma-phase Ni-Co

oxyhydroxides achieve ultrahigh mass/areal/volumetric energy density flexible all-solid-state asymmetric supercapacitor. *J. Mater. Chem. A.* **2023**, *11*, 5754-65. DOI

49. Jing, C.; Song, X.; Li, K.; et al. Optimizing the rate capability of nickel cobalt phosphide nanowires on graphene oxide by the outer/inter-component synergistic effects. *J. Mater. Chem. A.* **2020**, *8*, 1697-708. DOI
50. Zhang, Y.; Sun, L.; Zhang, L.; et al. Highly porous oxygen-doped NiCoP immobilized in reduced graphene oxide for supercapacitive energy storage. *Compos. Part. B. Eng.* **2020**, *182*, 107611. DOI
51. Wang, M.; Zhong, J.; Zhu, Z.; et al. Hollow NiCoP nanocubes derived from a Prussian blue analogue self-template for high-performance supercapacitors. *J. Alloys. Compd.* **2022**, *893*, 162344. DOI
52. He, S.; Li, Z.; Mi, H.; et al. 3D nickel-cobalt phosphide heterostructure for high-performance solid-state hybrid supercapacitors. *J. Power. Sources.* **2020**, *467*, 228324. DOI
53. Zhang, X.; Wu, A.; Wang, X.; Tian, C.; An, R.; Fu, H. Porous NiCoP nanosheets as efficient and stable positive electrodes for advanced asymmetric supercapacitors. *J. Mater. Chem. A.* **2018**, *6*, 17905-14. DOI
54. Zhang, X.; Zhang, L.; Xu, G.; Zhao, A.; Zhang, S.; Zhao, T. Template synthesis of structure-controlled 3D hollow nickel-cobalt phosphides microcubes for high-performance supercapacitors. *J. Colloid. Interface. Sci.* **2020**, *561*, 23-31. DOI
55. Fu, M.; Chen, W.; Lei, Y.; Yu, H.; Lin, Y.; Terrones, M. Biomimetic construction of ferrite quantum dot/graphene heterostructure for enhancing ion/charge transfer in supercapacitors. *Adv. Mater.* **2023**, *35*, e2300940. DOI
56. Pan, L.; Hu, R.; Zhang, Y.; et al. Built-in electric field-driven ultrahigh-rate K-ion storage via heterostructure engineering of dual tellurides integrated with $Ti_3C_2T_x$ MXene. *Nano-Micro. Lett.* **2023**, *15*, 225. DOI PubMed PMC
57. Wang, Q.; Yang, H.; Meng, T.; et al. Boosting electron transfer with heterointerface effect for high-performance lithium-ion storage. *Energy. Storage. Mater.* **2021**, *36*, 365-75. DOI
58. Li, P.; Han, Y.; Yan, F.; Yan, L.; Huang, H.; Zhou, W. Engineering NiCoP arrays by cross-linked nanowires and nanosheets as advanced materials for hybrid supercapacitors. *J. Energy. Storage.* **2021**, *38*, 102503. DOI
59. Gopalakrishnan, A.; Yang, D.; Ince, J. C.; Truong, Y. B.; Yu, A.; Badhulika, S. Facile one-pot synthesis of hollow NiCoP nanospheres via thermal decomposition technique and its free-standing carbon composite for supercapacitor application. *J. Energy. Storage.* **2019**, *25*, 100893. DOI
60. Gu, J.; Sun, L.; Zhang, Y.; et al. MOF-derived Ni-doped CoP@C grown on CNTs for high-performance supercapacitors. *Chem. Eng. J.* **2020**, *385*, 123454. DOI